Modular Isolated LLC DC/DC Conversion System for Offshore Wind Farm Collection and Integration

Hu, Pengfei; Yin, Rui; Wei, Baoze; Luo, Yongjie; Blaabjerg, Frede

Published in:
I E E E Journal of Emerging and Selected Topics in Power Electronics

DOI (link to publication from Publisher):
10.1109/JESTPE.2021.3062677

Creative Commons License
Unspecified

Publication date:
2021

Document Version
Accepted author manuscript, peer reviewed version

Modular Isolated LLC DC/DC Conversion System for Offshore Wind Farm Collection and Integration

Pengfei Hu, Member, IEEE, Rui Yin, Baoze Wei, Member, IEEE, Yongjie Luo, Member, IEEE, Frede Blaabjerg, Fellow, IEEE

***Abstract*—Compared with conventional offshore wind farm with ac collection and high-voltage dc (HVDC) transmission system, the offshore wind farm with all dc system shows advantages with characteristics of higher power density, lower costs and higher efficiency in many analyses. This paper proposed a novel all dc system for the offshore wind farm collection and integration. The presented dc system is composed of several medium-voltage (MV) dc collection systems and a dc transmission system. A novel Modular Isolated DC/DC Converter (MIDC) topology is proposed for the MV dc collection system to raise the medium dc voltage to a higher level, while realizing the Maximum Power Point Tracking (MPPT) of the connected wind generators. Thorough comparisons of three DC/DC converter candidates are carried out, and the LLC resonant converter is found to be the optimal Sub Module (SM) of the MIDC. Furthermore, a two-layer control system for the MIDC is developed to obtain current and voltage sharing while achieving the MPPT of the wind generators in the meantime. A time-domain simulation model consists of 160 SMs is developed by using PSCAD, and a prototype with 9 SMs is built for the experiments. The feasibility of the proposed pure dc system is verified by both the simulation and experimental results.**

***Index Terms*—Offshore wind farm, modular isolated DC/DC converter, power collection and transmission, HVDC.**

I. Introduction

HVDC may be the only feasible solution for power integration of the offshore wind farms that far away from the coastline [1-6]. The conventional collection and transmission system use bulky line frequency transformers to raise the voltage and decrease transmission losses. As the power rating of the offshore wind farm continues to grow, there is a dramatic increase in the cost of the platforms for line frequency transformers and the converter station. Moreover, it is extremely difficult to build the converter station platform, to transport and install these heavy and bulky transformers at sea [7], [8]. To overcome these drawbacks, the pure dc system has been proposed for the collection and transmission of the offshore wind farm, which exhibits lower costs, higher efficiency and higher power density than conventional ac collection system [9-13].

As the most important equipment in the pure dc system, the DC/DC converter has been studied by many researchers, and a variety of converter topologies have been proposed. In [14] and [15], the efficiencies of multiple conventional DC/DC converter topologies have been compared, including the hard switched Full Bridge (FB) converter, the FB converter with phase-shift control, the Single Active Bridge (SAB) converter, the Dual Active Bridge (DAB) converter, the series resonant converter, the parallel resonant converter and the LCC resonant converter. According to the results shown in [14] and [15], the FB converter with phase-shift control and the LCC resonant converter behave the characteristic of the lowest power losses among these topologies. The series and parallel connection of IGBTs is unavoidable when applying the above-mentioned conventional topologies in the offshore wind farm. Hence, the voltage and current sharing problem will limit their applications.

The modular DC/DC converter seems to be a smart choice for high voltage and high-power applications since the rated voltage and power of a single converter is limited [16], [17]. The Multilevel Modular DC Converter (M2DC) is proposed in [18] and a comprehensive study of the efficiency of this converter is done in [19]. Analysis in [8] demonstrates that the M2DC is not suitable for the scenario where high voltage gain is required. Therefore, it is not well suited for offshore wind farms. In [20], [21] and [22], three different modular DC/DC converters are proposed, which use the DAB converter, boost single switch converter and FB converter with phase-shift control as the SMs, respectively. The boost single switch converter does not have galvanic isolation between its low-voltage side and high-voltage side, resulting in decreased reliability of the offshore wind farm. There is galvanic isolation of DAB converter. However, the power transmission in an offshore wind farm is unidirectional most of the time, therefore, using DAB converter as the SM of the modular DC/DC converter is uneconomic and will cause additional power losses.

Although the modular DC/DC converter for offshore wind farm applications have been studied in many literatures, a systematic analysis of the SM topology is still rare. To ensure good performance, the topology of the SM should meet the following requirements:

(1) A unidirectional topology is more suitable for the SM since the power transmission in the offshore wind farm is unidirectional under normal operation.

(2) For safety and reliability considerations, a transformer-based galvanic isolation topology is desirable for the pure dc systems.

(3) The input voltage of the modular DC/DC converter will follow the variation of the output voltage of the wind turbine generator if a diode-based rectifier is connected between them. Hence, the SM should accommodate a fairly wide input voltage range.

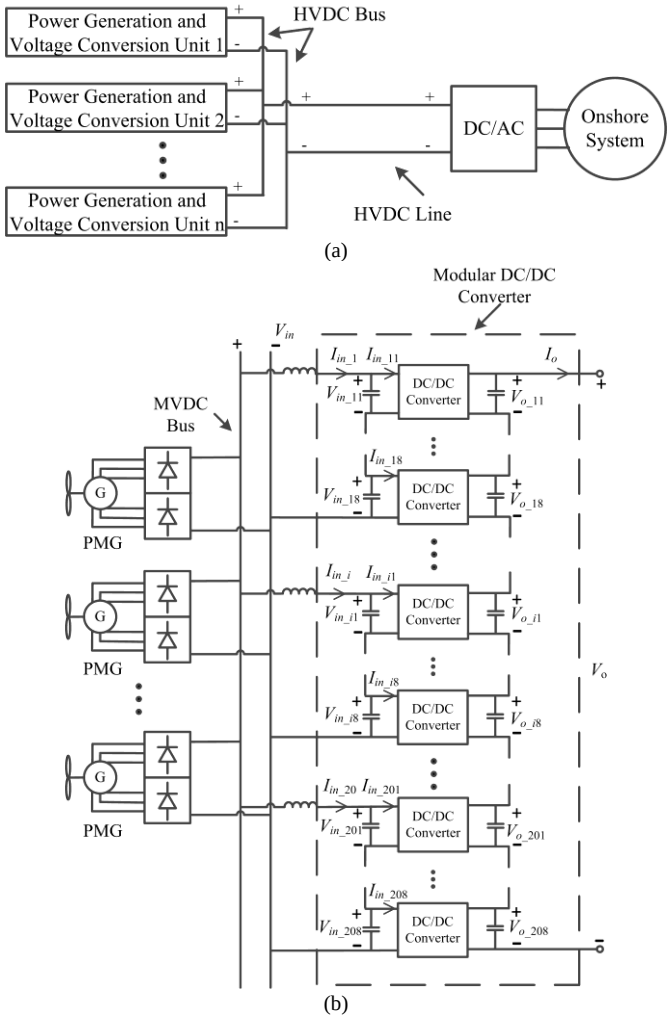

Fig. 1. The structure of the proposed pure dc system. (a) Full offshore DC wind farm. (b) Configuration of Power Generation and Voltage Conversion (PGVC) unit.

Among the multiple DC/DC converter topologies, the FB converter with phase-shift control and the LCC resonant converter under Discontinuous Current Mode (DCM) have the lowest power losses [14], [15], [22] while meeting the above requirements of the SM topology. Thus, these two topologies are taken into consideration in this paper. Besides, the LLC series-parallel resonant converter exhibits some excellent features, such as zero voltage and zero current switching, and high efficiency in a wide output power range [23]-[25]. Furthermore, it is also suitable for the scenario where the SM has a fairly wide input voltage range. For these reasons, the LLC topology operating in Continuous Current Mode (CCM) is considered as well.

In this paper, the abovementioned three candidates are compared thoroughly, and the LLC resonant converter is found to be the optimal topology of the concerned MIDC. Accordingly, a novel pure dc system is proposed for the offshore wind farm collection and integration based on the MIDC. The MIDC is aiming to boost the terminal voltage of the wind turbine generator to the transmission level while realizing the MPPT of the wind generators. Different from other papers merely focusing on the modular DC/DC converter, this paper takes the output characteristics of the Permanent Magnet Generators (PMGs) into consideration during the design of the MIDC parameters and the corresponding control system. A two-layer control architecture is proposed to realize the current and voltage sharing of the MIDC and the MPPT of the wind generators. Finally, a PSCAD simulation model with 160 SMs is developed, and an experimental prototype with 9 SMs is built to verify the proposed topology and control strategy.

II. System Configuration

The structure of the proposed pure dc system is shown in Fig. 1(a), which is comprised of several PGVC units, an HVDC line and a voltage source inverter. The PGVC unit consists of several PMGs and an MIDC, as shown in Fig.1 (b). In the concerned system, the offshore wind farm consists of 50 PMGs equally divided into 10 units, with each unit consisting of five adjacent MV 8-MW PMGs and one 40-MW MIDC. The PMGs in each unit are connected to the MVDC bus through their corresponding diode rectifiers, while the output side of the MIDC is connected to the HVDC bus shown in Fig. 1(a). To decrease the harmonic magnetomotive forces of the PMG, dual three-phase PMG is used, which has a 30° displacement between its two sets of three-phase stator windings [26]. The MIDC boosts the MVDC to 400 kV for long distance power transmission. As shown in Fig. 1(b), the MIDC consists of 160 SMs equally divided into 20 groups with each group consisting of 8 SMs. The 20 SM groups are connected in parallel at the input side and in series at the output side. A small smoothing inductor is used at the input side of the SM group to filter the high-frequency harmonics of the input current. Within each SM group, 8 SMs are connected in series both at the input side and output side in order to reduce the voltage ratings of the IGBTs and diodes of each SM.

Compared with the voltage source converter, the diode rectifier of the PMG has advantages of lower cost, higher efficiency and higher reliability. Considering that the PMGs in the same unit are adjacent, thus the wind speeds at the locations of these PMGs are similar. Consequently, the MPPT of the wind generators in the same unit can be realized by proper control of the MIDC.

The proposed system shows some other advantages, such as:

1) The transportation and installation cost of the offshore devices are reduced significantly as the proposed system eliminates the bulky and heavy line frequency transformer. Furthermore, the MIDC does not need any specialized platform and can be installed on the platform of the wind turbine because of its small size and light weight.
2) The novel structure of the proposed MIDC offers numerous merits, including high reliability, easy-to-realize redundancy as well as standardized design and production. As each single SM does not need to withstand very high DC voltage, 1.7 kV IGBTs can be used without series connection, which results in higher operating frequency of

the SM. The volume and weight of the medium-frequency transformer in the SM can thus be reduced.

3) The losses in the collection grid of the pure dc system is much lower compared with the conventional offshore wind farm since the MIDC is very close to the PMGs in its unit.

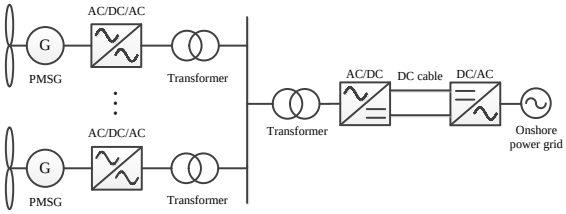

Fig. 2 Conventional offshore wind farm HVDC transmission system

An economic comparison is made between the proposed system and the conventional offshore wind farm HVDC transmission system, shown in Fig.2. Since many AC/DC and DC/AC converters are employed, it is really difficult to compare the switch counts and losses comprehensively. As a rough comparison, the capacity of the wind turbine is taken as an index, which is assumed to be *P* and the wind turbine number is *k*. Since both the topology in Fig.2 and the proposed one in this paper are full power conversion system by power converters, the rated converter capacity is equal to the total wind turbine capacity. Thus, the converter capacity comparison can be made comprehensively. As well, other aspects including the fundamental frequency transformer, medium frequency transformer and offshore platform are analyzed. The detailed comparison results are shown in Table I, where it can be seen that the proposed topology needs only *kP* power capacity of converters without offshore platform.

TABLE I
COMPARISON OF THE PROPOSED TOPOLOGY AND THE CONVENTIONAL ONE

	Conventional Topology	Proposed Topology
AC/DC converter	2*kP*	*kP*
DC/AC converter	*kP*	0
DC/DC converter	0	*kP*
Fundamental frequency transformer	need	/
Medium frequency transformer	/	need
Offshore platform	need	/

III. COMPARISONS OF DIFFERENT DC/DC CONVERTER TOPOLOGIES

In this section, the FB converter with phase-shift control, the LCC and LLC resonant converters are compared in detail.

A. Circuits and their corresponding parameters of three DC/DC converters

The circuit diagrams of the concerned three topologies are shown in Fig.3. The main circuit parameters of these topologies are designed according to [27] and [28] and listed in Table II and Table III, respectively. For all these three topologies, the transformer core is comprised of two C-cores and the METGLAS alloy 2705M is chosen as the material.

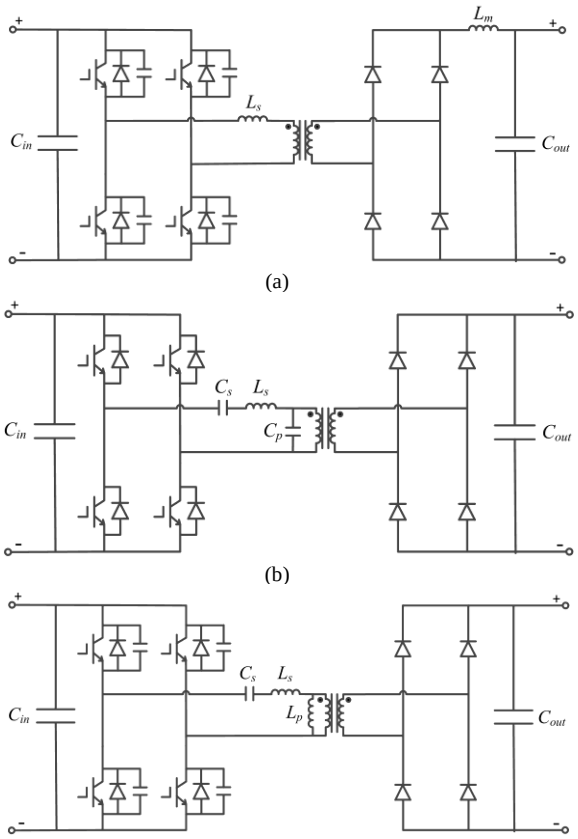

Fig. 3. Circuit diagrams of the DC/DC converters. (a) FB converter using phase-shift control. (b) LCC resonant converter. (c) LLC resonant converter.

TABLE II
MAIN PARAMETERS OF THREE DC/DC CONVERTER TOPOLOGIES IN FIG.3

	FB	LCC	LLC
Input voltage	0.39-1 kV	0.39-1 kV	0.39-1 kV
Output voltage	2.5 kV	2.5 kV	2.5 kV
Input power	0.008-0.25 MW	0.008-0.25 MW	0.008-0.25 MW
Frequency	5 kHz	0.45-5.12 kHz	3.01-5.17 kHz
C_{in}	200 μF	250 μF	250 μF
C_{out}	5 μF	100 μF	100 μF
Other parameters	L_s=7.5 μH L_m=5 mH	C_s=25 μF C_p=3.4 μF L_s=9.7 μH	C_s=9.2 μF L_s=76.2 μH L_p=381.1 μH

TABLE III
PARAMETERS OF THE MEDIUM-FREQUENCY TRANSFORMERS IN FIG.3

	FB	LCC	LLC
Current density	6 A/mm^2	6 A/mm^2	6 A/mm^2
Number of turns	3;30	8;80	14;32
Turn Ratio	1:10	1:10	1:2.3
Core Volume	0.0147 m^3	0.1413 m^3	0.0191 m^3

B. Comparison of topologies

In this subsection, the component stresses, component counts and losses are compared for the topologies. To compare the component stresses of the three topologies, simulation models based on PSCAD/EMTDC are built, and the simulation results are given in Table IV.

TABLE IV
COMPONENT STRESSES OF THREE DC/DC CONVERTER TOPOLOGIES IN FIG. 3

	FB	LCC	LLC
IGBT module peak current	1.085 kA	2 kA	0.45 kA
IGBT module RMS current	0.67 kA	0.84 kA	0.21 kA
IGBT module peak voltage	1 kV	1 kV	1 kV
Rectifier diode peak current	0.109 kA	0.199 kA	0.186 kA
Rectifier diode RMS current	0.067 kA	0.084 kA	0.084 kA
Rectifier diode peak voltage	9 kV	2.5 kV	2.5 kV

Due to zero voltage turn-off switching in all three converters and as can be seen from Table IV, IGBT modules rated at 1.7 kV can be used in all three converters. According to the simulation results in Table IV, Infineon FZ1200R17HE4 rated at 1.7 kV and 1.2 kA, FZ2400R17HE4_B9 rated at 1.7 kV and 2.4 kA and FF450R17ME4 rated at 1.7 kV and 0.45 kA are chosen as the IGBT modules for the FB converter, the LCC resonant converter and the LLC resonant converter, respectively. For the rectifier diodes, Infineon DZ800S17K3 with voltage and current ratings of 1.7 kV and 0.8 kA is used for all the topologies. To accommodate the diode peak voltages of the output rectifier listed in Table IV, three DZ800S17K3 in series connection are required for the LCC and LLC converters, and ten DZ800S17K3 for the FB converter. Table V shows the component counts for the topologies.

According to the designed parameters and selected components above, the concerned winding and core losses, semiconductor conduction and switching losses are obtained through PLECS-based simulations. Fig.4 shows the efficiencies of the three topologies and Fig.5 shows the breakdown of the losses.

TABLE V
COMPONENT COUNTS OF THREE DC/DC CONVERTER TOPOLOGIES IN FIG. 3

	FB	LCC	LLC
Number of IGBTs	4	4	4
Number of rectifier diodes	40	12	12

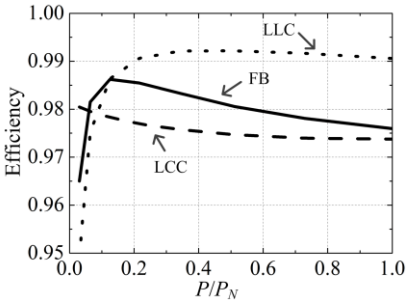

Fig. 4. Efficiencies of three DC/DC converter topologies in Fig. 3

In comparison with LLC and LCC resonant converters with Pulse Frequency Modulation (PFM), designing the transformer of the FB converter with phase-shift control is easier due to its constant operating frequency. As shown in Table III, the transformer of the FB converter has the smallest core volume and area product among the three topologies. However, there is a large smoothing filter inductor at the output of the FB converter, which increases its total volume and weight. The peak current of the IGBT module and the peak voltage of the rectifier diode are high. Hence, the current rating of the IGBT module and the number of rectifier diodes are also high accordingly, resulting in a higher total cost. Additionally, according to the analysis in [16], the FB converter in this scenario cannot realize soft switching in its lagging leg switches. Therefore, the semiconductor loss of this topology is higher than that of the other two topologies, as shown in Fig.5.

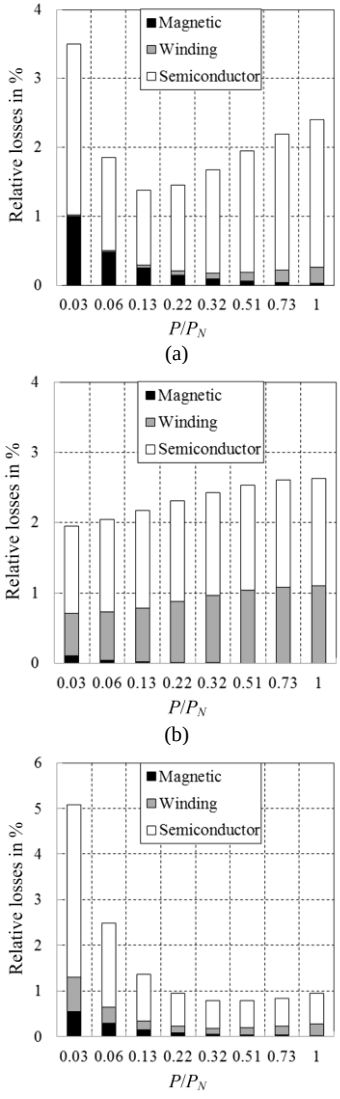

Fig. 5. Losses of three DC/DC converter topologies. (a) FB converter using phase-shift control. (b) LCC resonant converter. (c) LLC resonant converter.

The LCC resonant converter is operated in DCM. Although the DCM ensures IGBT modules soft switching all the time, it also leads to a large resonant current in the resonant tank, which will cause high semiconductor conduction losses and high transformer winding loss, as shown in Fig.5 (b). The IGBT module used for the LCC resonant converter has the highest current rating among all three topologies, resulting in significantly higher component cost. Moreover, as shown in Table III, the core volume and area product of the LCC resonant converter transformer are much larger than that of the other two topologies. Based on the above analysis, a conclusion can be drawn that the LCC resonant converter under DCM is not suitable for the MIDC.

The LLC resonant converter is operated in CCM. Though the PFM is used for both LLC resonant converter and LCC resonant converter, the operating frequency range of the LLC resonant converter is narrower. The core volume and area product of the LLC resonant converter transformer are slightly larger than

those of the FB converter transformer. However, the large smoothing inductor used in the FB converter output filter is not required for the LLC resonant converter. As shown in Table IV, the peak and RMS currents of the IGBT module of the LLC resonant converter are much smaller than those of the other two topologies, which can reduce the component cost. The semiconductor conduction loss and winding loss of this topology are lower as well. The IGBT module can realize zero-current turn-on switching and nearly-zero-voltage turn-off switching all the time. Taking all of these into consideration, the efficiency of the LLC resonant converter can be very high. As shown in Fig. 4 and Fig. 5 (c), within most of the operation range, the efficiency of the LLC resonant converter is much higher than that of the other two topologies. As a conclusion, the LLC resonant converter operated in CCM has lower cost, smaller volume and higher efficiency compared with the FB converter with phase-shift control and the LCC resonant converter operated in DCM. Therefore, the LLC resonant converter is chosen as the SM topology of the MIDC.

IV. Control System

In this section, a two-layer control architecture is developed, which is comprised of one top-layer controller and 160 bottom-layer controllers corresponding to the 160 SMs. The top-layer controller is used to regulate the input current sharing among the SM groups, while ensuring the MPPT of the wind generators. The bottom-layer controller is used to regulate the input voltage sharing within each SM group. The configuration of the two-layer control system is shown in Fig. 6.

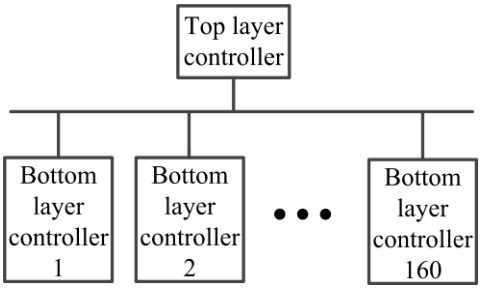

Fig. 6. Configuration of the two-layer control system for the whole system.

A. Operation curve-voltage gain VS operating frequency

The voltage gain versus operating frequency of the LLC resonant converters within the whole output power range of the wind generator is critical for the proper design of its control algorithm.

The voltage gain of the LLC resonant converter can be written as [28]

$$M=\frac{V_{o\_ij}}{n_t V_{in\_ij}}=\left|\frac{(\frac{\omega^2}{\omega_o^2})\sqrt{m(m-1)}}{(\frac{\omega^2}{\omega_p^2}-1)+j(\frac{\omega}{\omega_o})(\frac{\omega^2}{\omega_o^2}-1)(m-1)Q^e}\right| \quad (1),$$

where M is the voltage gain, ω is the operation angular frequency, ω_o and ω_p are the resonant angular frequencies determined by L_p, L_s and C_s, m is the ratio between L_p+L_s and L_s, n_t is the turn ratio of the medium-frequency transformer, V_{o_ij} is the output voltage of the j^{th} SM in the i^{th} SM group, V_{in_ij} is the input voltage of the j^{th} SM in the i^{th} SM group, i=1, 2,…, 20, j=1, 2,…, 8. Q^e is the equivalent quality factor, which is determined by the input power of the LLC resonant converter [28]. Based on the parameters listed in Table I, Fig. 7 shows the voltage gain curves of the LLC resonant converter for different Q^e with f_o=6 kHz, m=6, where f_o is the resonant frequency corresponding to ω_o.

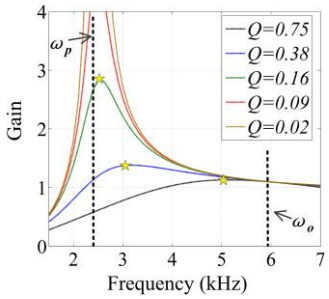

Fig. 7. Voltage gain curves of LLC resonant converter.

As shown in Fig. 7, not only ω but also Q^e has an influence on the voltage gain of the LLC resonant converter. Since the PMG is connected to the MVDC bus through a diode-based rectifier, the input voltage of the SM varies with the PMG rotor speed. Assuming that the control system can realize voltage sharing at the output side of the SMs, and the output voltage of the SM is almost unchanged, as a result, the voltage gain of the LLC resonant converter varies with the rotor speed. Moreover, the input power of the SM also varies with the rotor speed because the MIDC regulates its input power according to the rotor speed to realize the MPPT control of the PMG. The variation of the SM input power is similar to the variation of Q^e, because Q^e is determined by the input power. Therefore, not only M but also Q^e varies with the rotor speed, which means that the position of the SM operating point is changing from one voltage gain curve to another. To get a precise operation curve of the LLC resonant converter, a detailed analysis is performed in the following part of this section.

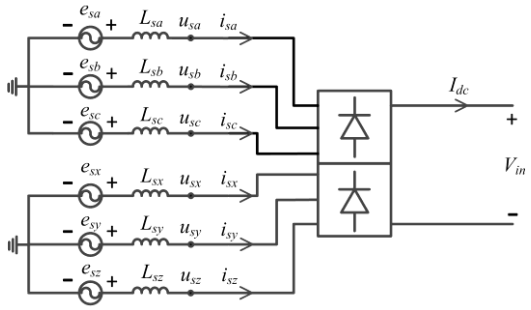

Fig. 8. Equivalent circuit of the PMG with the rectifier.

The equivalent circuit of the PMG with two sets of three-phase windings is shown in Fig.8, where e_s is the generator internal voltage, L_s is the synchronous inductance, u_s is the terminal voltage, i_s is the AC side current, I_{dc} is the DC side current and V_{in} is the DC side voltage. Assuming that the MIDC can realize the MPPT of the wind generators, the generator internal voltage and the output active power of a non-salient PMG are [29]

$$e_s=n_p\omega_r\psi_f \quad (2)$$

$$P_G=k_{opt}\omega_r^3=V_{in}I_{dc} \quad (3),$$

where n_p is the number of pole pairs, ω_r is the rotor speed, ψ_f is the excitation flux linkage generated by the permanent magnet, P_G is the active power output and k_{opt} is the optimum power

coefficient. According to (2) and (3), P_G can be expressed as

$$P_G = \frac{k_{opt}}{n_p^3 \psi_f^3} e_s^3 \quad (4).$$

Assuming that the voltage and current sharing of the MIDC can be guaranteed, the input power of the SM is

$$P_{in\_ij} = N_G P_G / (N_{group} N_{sm}) \quad (5),$$

where P_{in_ij} is the input power of one SM, N_G is the number of PMGs in one PGVC unit, N_{group} is the number of the SM groups and N_{sm} is the number of SM in one SM group.

Substituting (4) into (5) yields:

$$P_{in\_ij} = \frac{N_G k_{opt}}{N_{group} N_{sm} n_p^3 \psi_f^3} e_s^3 \quad (6).$$

According to the analysis in [28], Q^e can be expressed as

$$Q^e = \sqrt{\frac{L_s}{C_s}} \frac{\pi^2 m}{8n^2 (m-1) V_{o\_ij}^2} P_{in\_ij} \quad (7),$$

where n is the transformer ratio. Substituting (6) into (7) yields:

$$Q^e = \frac{\pi^2 m N_G k_{opt} \sqrt{L_s C_s}}{8n^2 (m-1) V_{o\_ij}^2 N_{group} N_{sm} n_p^3 \psi_f^3 C_s} e_s^3 = A e_s^3 \quad (8),$$

where

$$A = \frac{\pi^2 m N_G k_{opt} \sqrt{L_s C_s}}{8n^2 (m-1) V_{o\_ij}^2 N_{group} N_{sm} n_p^3 \psi_f^3 C_s}.$$

As shown in Fig.8, the synchronous inductance of the PMG can be seen as the commutation inductance of the diode rectifier. Assuming that the DC current is continuous, the voltage of the MVDC bus is expressed as

$$V_{in} = \frac{6\sqrt{3}}{\pi} e_s - \frac{6 n_p \omega_r L_s}{\pi} I_{dc} \quad (9).$$

According to (2), (3), (4) and (9), V_{in} can be rewritten as

$$V_{in} = \frac{1}{2}(B + \sqrt{B^2 - 4Ce_s^2}) e_s \quad (10),$$

where

$$B = \frac{6\sqrt{3}}{\pi}, \quad C = \frac{6 k_{opt} L_s}{\pi n_p^3 \psi_f^4}.$$

Therefore, the input side voltage of the SM can be expressed as

$$V_{in\_ij} = V_{in} / N_{sm} = \frac{1}{2N_{sm}}(B + \sqrt{B^2 - 4Ce_s^2}) e_s \quad (11).$$

The voltage gain of the SM is

$$M = \frac{V_{o\_ij}}{n_t V_{in\_ij}} = \frac{2N_{sm} V_{o\_ij}}{(B + \sqrt{B^2 - 4Ce_s^2}) e_s} \quad (12).$$

At steady state, A, B and C are constants. It is known from (8) and (12) that not only Q^e but also M is determined by e_s. Based on the values of e_s, the values of Q^e and M can be calculated. For any values of Q^e, the LLC resonant converter should be operated on the right side of the voltage gain curve to ensure soft switching of the IGBTs. For this reason, there is a one-to-one relationship between the values of Q^e and the values of M.

The operation curve of the LLC resonant converter in Fig.9, plotted according to the values of Q^e and M, shows that the voltage gains of the SM decreases with increasing operating frequency.

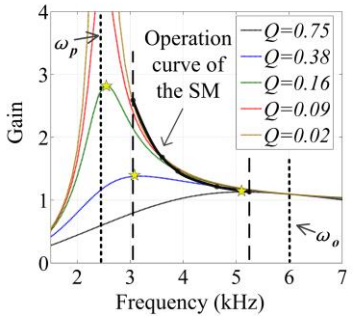

Fig. 9. Operation curve of the LLC resonant converter.

B. Controller design

Based on the above analysis, the bottom-layer controllers of one SM group are designed as shown in Fig.10, where V_{smref_i} is the reference value of the input voltage of the SMs in the i^{th} SM group, I_{in_ij} is the input current of the j^{th} SM in the i^{th} SM group and f_{ref_ij} is the reference value of the frequency of the j^{th} SM in the i^{th} SM group. As shown in Fig. 10, the reference values of the input voltage of the SMs in the same group are identical, which is generated by the top-layer controller. Hence, the input voltage sharing of the SMs in the same SM group can be achieved.

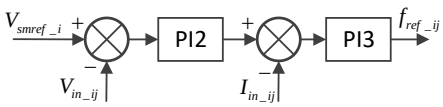

Fig. 10. Configuration of the j^{th} SM bottom-layer controller in the i^{th} group.

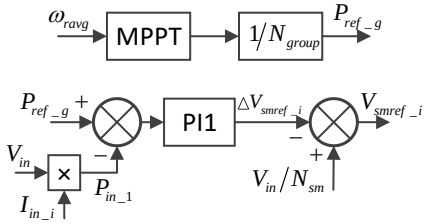

Fig. 11. Configuration of the i^{th} top-layer controller.

The top-layer controller is aimed to realize the MPPT of the wind generators, while achieving input current sharing among the SM groups. As shown in Fig. 1, the PMGs in the same PGVC unit are connected in parallel through diode rectifiers. Therefore, the rotor speeds of the PMGs in the same PGVC unit are very similar to each other during normal operation. The average value of the rotor speeds is used for the MPPT control of the PMGs. Fig. 11 shows the configuration of the top-layer controller, where ω_{ravg} is the average value of the rotor speeds. P_{ref} is the reference value of the MIDC input power, which is obtained according to the MPPT curve of the wind generators. P_{ref_g} is the reference value of the SM group input power, ΔV_{ref_i} is the power controlling component of V_{smref_i}, I_{in_i} and P_{in_i} are the input current and input power of the i^{th} SM group, respectively.

In the top-layer controller, ΔV_{ref_i} is used to realize the input power sharing of the SM groups, while V_{in}/N_{sm} is used to realize the input voltage sharing among the SMs in one SM group. The

reference value of the input voltage of the SMs in the i^{th} SM group is therefore given by

$$V_{smref\_i} = V_{in} / N_{sm} - \Delta V_{ref\_i} \quad (13).$$

It can be seen from Fig.11 that ΔV_{ref_i} is increased when the input power of the SM group P_{in_i} is smaller than its reference value P_{ref_g}, causing V_{smref_i} to decrease. According to the bottom-layer controller shown in Fig.10, the operating frequency f_{ref_ij} of the SM is then decreased. Since the voltage gain of the SM will increase with the decrease of the operating frequency as shown in Fig.9, the output voltage of the SM will increase accordingly. Therefore, the input power of the SM group is increased. Conversely, when the input power of the SM group is larger than its reference value, ΔV_{ref_i} is decreased, which will decrease the input power of the SM group. Through a PI regulator, the input power of each SM group can track the same reference value P_{ref_g}, which means that the input power sharing of the SM groups is realized. Since the inputs of the SM groups within one PGVC unit are connected to the same MVDC bus, the input power sharing control is equivalent to the input current sharing control. As P_{ref_g} is obtained according to the MPPT curve of the wind generators, the MPPT control of the wind generators is also realized. It is worth mentioning that the controller parameters in Fig.10 and Fig.11 are designed by simulation-based trial and error method and detailed controller design is a future scope of research. The specific controller parameters are shown in Appendix I Table A. II.

TABLE VI
DETAILED PARAMETERS OF MIDC FOR SIMULATION

items	values
Rated power	40 MW
Rated input voltage	8 kV
Rated output voltage	400 kV
Number of SM groups	20
Number of SMs	160
Number of SMs in one SM group	8
Smoothing inductance	100 μH

According to the analysis in [30], the output voltage sharing of the input-series-output-series system can be realized automatically as long as the control system achieves the input voltage sharing. Therefore, the output voltage sharing of the SMs in one SM group can be realized as long as the bottom-layer controller achieves the input voltage sharing of the SMs within its group. Literature [30] also indicates that the output voltage sharing of the input-parallel-output-series system can be realized automatically as long as the control system achieves the input current sharing. If one SM group can be seen as one unit, the MIDC can be seen as an input-parallel-output-series system. Therefore, the output voltage sharing among the SM groups can be realized as long as the top-layer controller achieves the input current sharing among the SM groups. In other words, the output voltage sharing of all the MIDC SMs can be realized automatically as long as the top-layer controller achieves the input current sharing among the SM groups and the bottom-layer controllers achieve the input voltage sharing among the SMs in their SM groups. As a result, it is unnecessary to design an additional controller to realize the output voltage sharing of the MIDC.

V. SIMULATION RESULTS

To verify the effectiveness of the control system, an MIDC model with 160 SMs is built in PSCAD/EMTDC, and the circuit diagram of the simulation model is shown as Fig.12. As the main purpose of the simulation model is to investigate the characteristics of the MIDC, the onshore voltage source converter is substituted by a DC voltage source. The five 8-MW PMGs in one PGVC unit are aggregated into a 40-MW PMG.

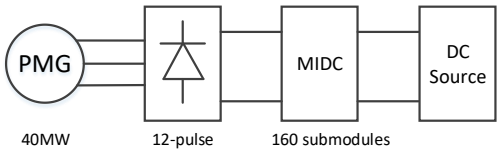

Fig. 12. Circuit diagram of the simulation model

Detailed parameters of the MIDC are listed in Table VI, while the parameters of the PMG and HVDC line are shown in Appendix I.

A. Steady state performances

Fig. 13 shows simulation results of the PGVC unit under the rated operating condition. The periodic fluctuations of V_{in} and I_{dc} shown in Fig.13 result from the harmonics generated by the diode rectifier. Thanks to the use of the dual three-phase PMG, the fluctuations of V_{in} and I_{dc} are limited within 1.6% and 5.5% of their rated values, respectively.

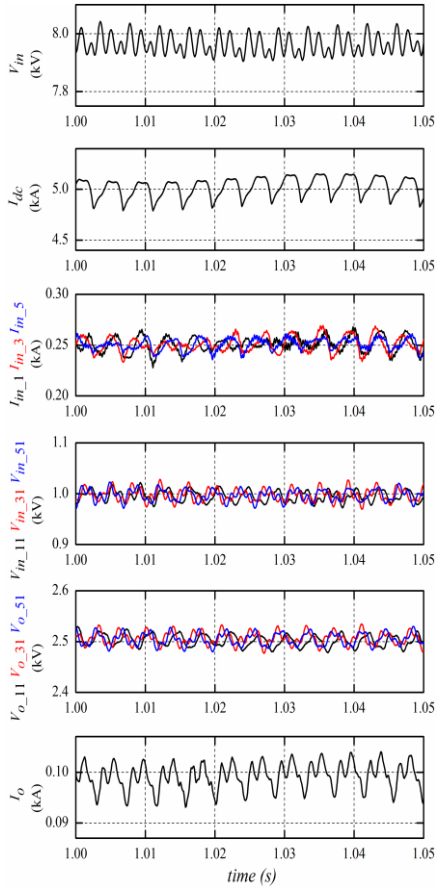

Fig. 13. Steady state performances of the MIDC.

One of the main objectives of the top-layer controller is to realize the input current sharing among the SM groups. The input currents of the first, third and fifth SM groups are shown

in Fig. 13, which verifies the effectiveness of the top-layer controller. Fig. 13 also depicts the input voltages of the first SMs in the first, third and the fifth SM groups, which proves that the input voltage sharing within the SM group can be achieved by the bottom-layer controller. According to the analysis in Section IV, once the top-layer controller achieves input current sharing among the SM groups and the bottom-layer controllers achieve input voltage sharing within the SM groups, the output voltage sharing of all the SMs can be realized accordingly. The output voltages of the SMs shown in Fig.13 validate the theoretical analysis.

B. *Transient performances*

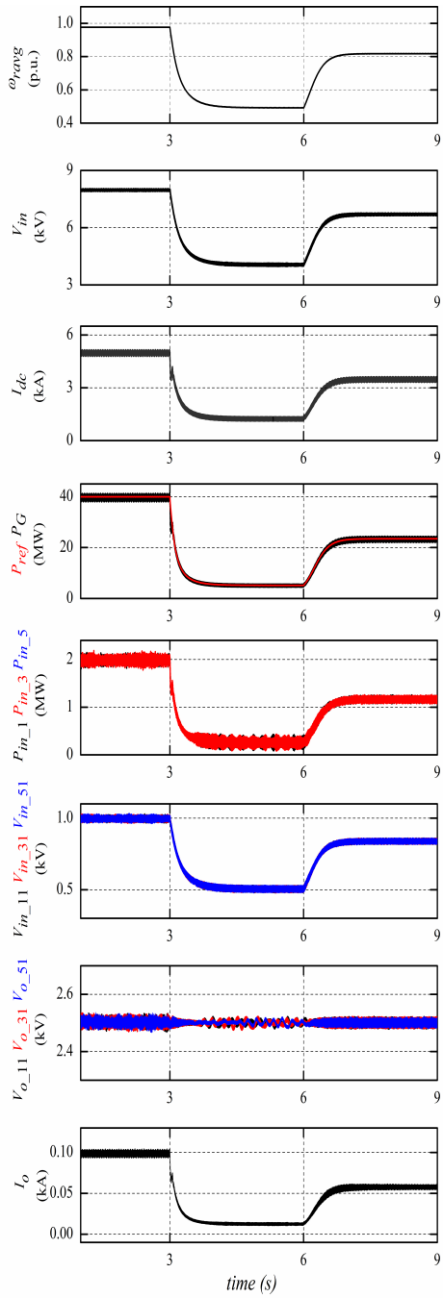

Fig. 14. Transient performances of the PGVC unit.

The transient performances of the system are illustrated in Fig. 14. At the beginning, the wind velocity is 12 m/s. At t=3s, the wind velocity decreased to 6 m/s, kept constant for 3s, and then increased to 10 m/s. During the whole process, the input power sharing of the SM groups and the voltage sharing of the SMs are well controlled by the presented control system. Meanwhile, the input power P_G of the MIDC can follow its reference value P_{ref} quickly without overshoot. Since P_{ref} is generated according to the MPPT curve of the wind generators, the MPPT of the wind generator is realized as well.

VI. Prototype and Experimental Results

A. *Experimental system configuration*

To verify the feasibility of the system proposed in this paper, a multi-terminal dc experimental system containing an MIDC prototype with 9 SMs is built, as shown in Fig. 15. A total of six PGVC units are emulated. One PGVC unit shown in Fig. 1(b) is built by a power amplifier and an MIDC prototype, while other five PGVC units in the offshore wind farm are represented by a Voltage Source Rectifier (VSR). The onshore DC/AC converter is represented by a Voltage Source Inverter (VSI).

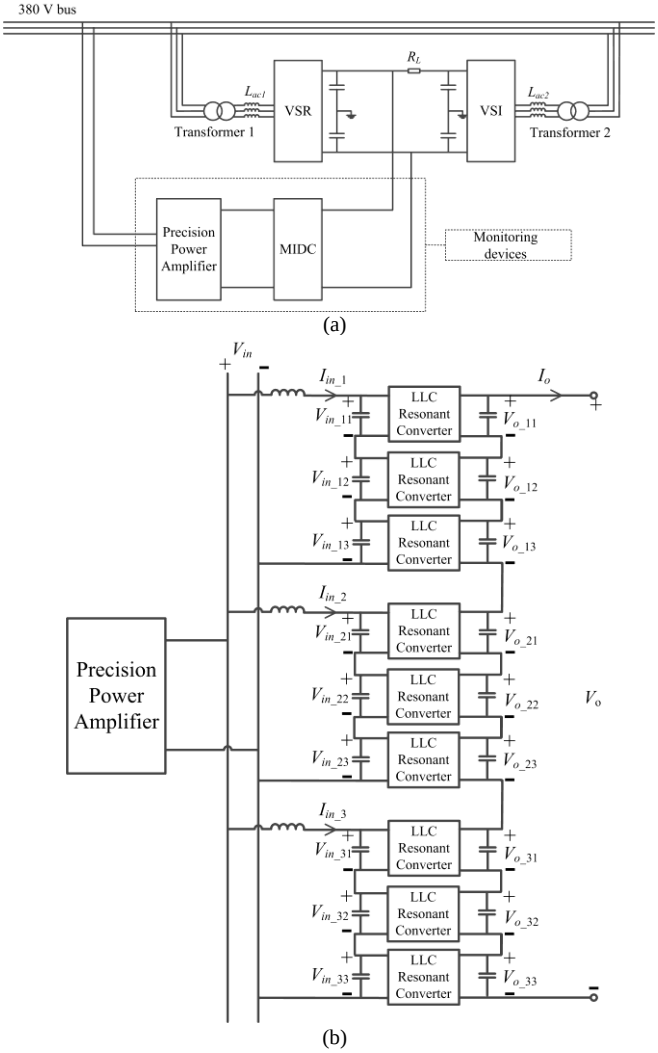

Fig. 15. Configuration of the experimental system. (a) Configuration of the multi terminal DC experimental system. (b) Configuration of the PGVC unit.

As shown in Fig. 15, the VSR ac side and VSI ac side are connected to the same 380V ac bus through two ac inductors (L_{ac1} and L_{ac2}) and two isolation transformers (Transformer 1 and Transformer 2), while their DC side contains four capacitors and a small resistor (R_L) representing the DC transmission line. The PGVC unit consists of a power amplifier

and an MIDC. A mathematical model of the PMG and its diode-based rectifier is implemented by using the NI CompactRIO, which is also used as the top-layer controller of the MIDC prototype. The NI CompactRIO will output an analog voltage signal according to the mathematical model. Then the analog signal will be amplified by the power amplifier whose output is connected to the input of the MIDC. The mathematical model of the PMG and its diode-based rectifier that built in the NI CompactRIO is described in the following Appendix II. Detailed parameters of the experimental system are listed in Table VII and the prototype of the system is shown in Fig. 16 and Fig. 17.

TABLE VII
DETAILED PARAMETERS OF THE EXPERIMENTAL SYSTEM

	items	values
MIDC	Rated power	1 kW
	Input voltage range	30~135 V
	Rated output voltage	750 V
	Rated frequency	50 kHz
	Number of SM groups	3
	Total number of SMs	9
	Number of SMs in one SM group	3
	Smoothing inductor	1 mH
SM	Rated power	110 W
	Input voltage range	10~45 V
	Rated output voltage	83.3 V
	Operating frequency range	25~50kHz
	Input side capacitor of SM	100 μF
	Output side capacitor of SM	940 μF
	Series resonant capacitor of SM	0.68 μF
	Series resonant inductor of SM	15μH
	Parallel resonant inductor of SM	96 μH
	Ratio of transformer	1:1.8
Power Amplifier	Rated Power	2.55 kW
	Rated out voltage	170 V
	Gain	100 V/V
VSR and VSI	Rate AC side line-line voltage	380V
	Rated DC side voltage	750 V
	Rated frequency	50Hz
	AC inductor	0.5 mH
	DC side capacitor	1200 μF

B. *Control system of the MIDC prototype*

Fig. 18 shows the configuration of the two-layer control system of the MIDC. As it has been mentioned before, the top-layer controller, NI CompactRIO by National Instruments, is used to realize the input current sharing of the SM groups and the MPPT of the wind generator. The NI CompactRIO consists of an embedded real-time controller, a reconfigurable FPGA card and multiple I/O modules. TMS320F28335 DSP by TI is used in the bottom-layer controller, which realizes the input voltage sharing within each SM group. The input voltage reference value V_{smref_i} is generated by the top-layer controller for each SM group and then transmitted to the bottom-layer controllers through a 16-bit high-speed I/O bus.

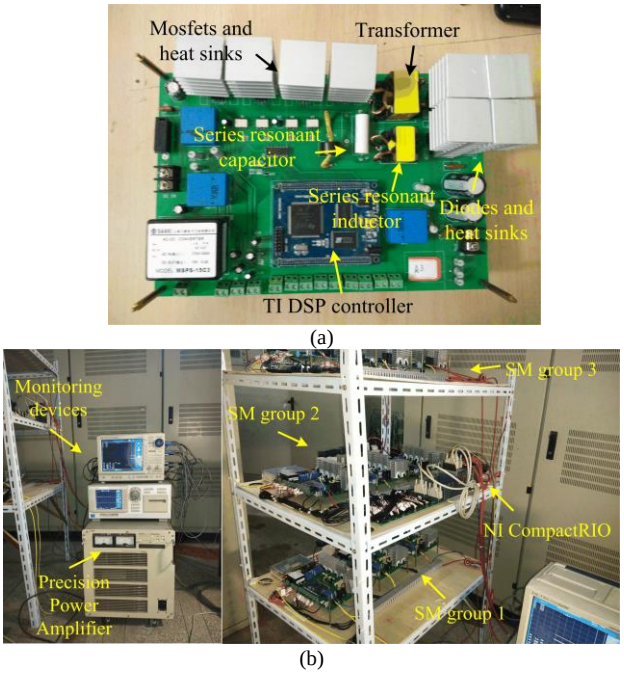

Fig. 16. Hardware system: (a) The SM board. (b) The MIDC prototype, power amplifier and monitoring devices.

Fig. 17. Prototypes of the VSR and VSI.

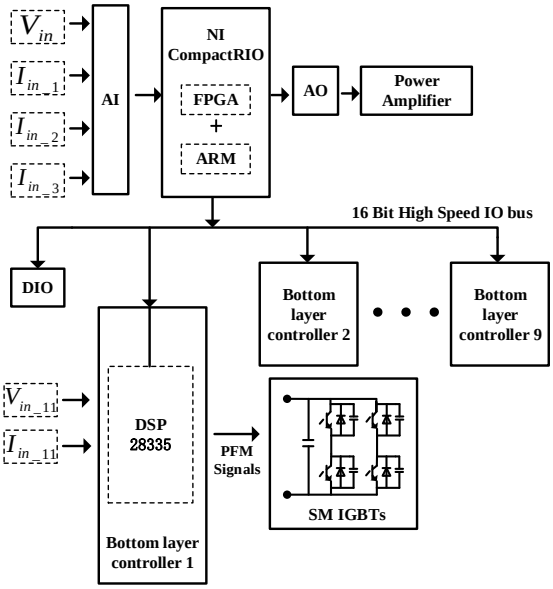

Fig. 18. Configuration and implementation of the MIDC control system.

C. Steady state performances

Fig. 19 depicts the steady state performances of the MIDC prototype. The DC side output power of the VSR is 5 kW, which is to emulate five PGVC units operated at rated power. The wind speed in the PMG mathematical model is configured as 8 m/s. Fig. 19(a) illustrates the input voltages of the first SMs in three SM groups. Fig. 19(b) shows the output voltages of the first SMs in three SM groups and Fig. 19(c) depicts the input currents of the three SM groups. From Fig. 19, both the input current sharing among the SM groups and the input and output voltage sharing among the SMs are well achieved, which demonstrates the effectiveness of the proposed control system.

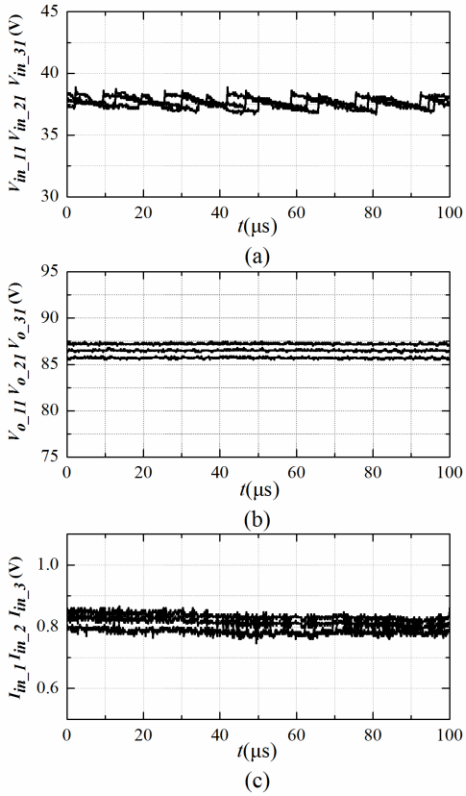

Fig. 19. Measured steady state performances of MIDC prototype. (a) Input voltages of the 1th SMs in three SM groups. (b) Output voltages of all SMs. (c) Input currents of three SM groups.

D. Transient performances

Fig. 20 and Fig. 21 show the transient performances of the experimental system. The output power of the VSR is 5 kW, while the VSI regulates its DC side voltage at 750 V. The wind speed in the PMG mathematical model is increased from 9 m/s to 10 m/s at t=30 s and then decreased to 8 m/s at t=70 s. Fig. 20(a) and Fig. 20(b) show the input voltages of the first SMs in three SM groups and output voltages of all the SMs, respectively. The input currents of the three SM groups are shown in Fig. 20(c). During the whole transients, current sharing and voltage sharing of the MIDC are well controlled. The three curves in Fig. 21 illustrate the input voltage V_{in}, the output voltage V_o and the input power P_G of the MIDC, respectively. The start-up sequence is as follow: first, charging the high-voltage DC side to its rated value via VSI in Fig.15; second, increasing the input voltage and input power based on a constant rotation speed of PMSG; third, switching to MPPT control of the PMSG. Fig. 22 shows the start-up process of the output voltage V_{out} of MIDC, which reaches 750 V after about 60 seconds.

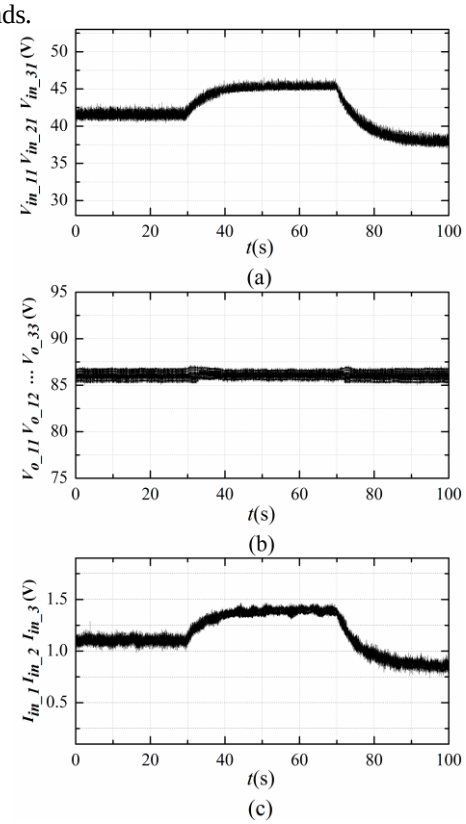

Fig. 20. Measured transient performances of the MIDC prototype. (a) Input voltages of the first SMs in three SM groups. (b) Output voltages of all SMs. (c) Input currents of three SM groups.

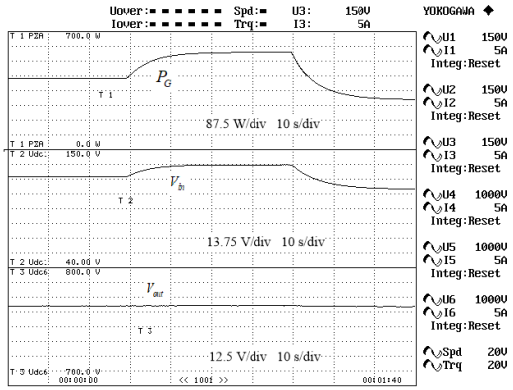

Fig. 21. Input power P_G, input voltage V_{in} and output voltage V_{out} of MIDC during transients.

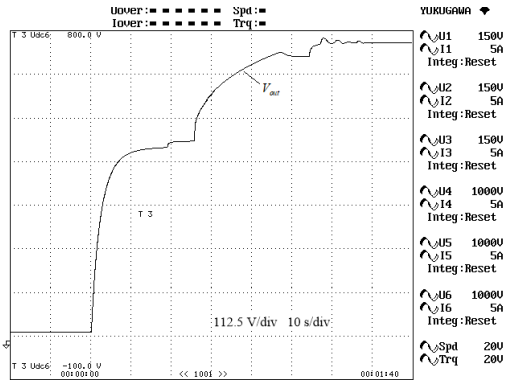

Fig. 22. Output voltage V_{out} of MIDC during start-up process.

VII. Conclusion

In this paper, an offshore wind farm with all dc collection and transmission system has been presented. A modular isolated DC/DC converter is proposed to boost the MVDC voltage to transmission level while also realizing the MPPT of the wind generators. A systematic analysis of the SM topology of the MIDC is done, and the LLC resonant converter is chosen as the SM for the MIDC. A two-layer control architecture consisting of one top-layer controller and one hundred and sixty bottom-layer controllers is developed, which achieves current and voltage sharing of the MIDC and the MPPT of the wind generators. Simulation and experimental results verify the feasibility of the proposed offshore wind farm and the effectiveness of the MIDC control system.

As the bulky line frequency transformers and large converter station are not required, the investment cost of the offshore wind farm is reduced significantly. As the efficiency of the MIDC is approximately 99% within most of its operation range and the efficiency of the diode-based rectifier is also very high, the total efficiency of the proposed system is obviously higher than that of the conventional offshore wind farm, which makes it more competitive

Appendix I

Table A.I Parameters of PMG and HVDC Line

	items	values
PMG	Rated power	40 MW
	Rated voltage	2.96 kV
	Frequency	20 Hz
	Number of poles	150
	Stator resistance	0.01 pu
	d-axis reactance of 1st winding set	1.0 pu
	q-axis reactance of 1st winding set	1.0 pu
	d-axis reactance of 2nd winding set	1.0 pu
	q-axis reactance of 2nd winding set	1.0 pu
	Field flux	1.0 pu
HVDC cable (100 km)	Resistance	3.4 Ω
	Inductance	12 mH

Table A.II Controller Parameters of the System

items	values
K_{P1}	0.0003
K_{I1}	0.1
K_{P2}	1
K_{I2}	1
K_{P3}	0.5
K_{I3}	50

Appendix II

The mathematical model of the wind generator and its corresponding rectifier can be fully described by the following equations.

$$\lambda = \omega_r R / v \tag{14}$$

$$\lambda_i = \frac{1}{1/(\lambda + 0.08\beta) - 0.035/(\beta^3 + 1)} \tag{15}$$

$$C_p = 0.22(116/\lambda_i - 0.4\beta - 5)e^{-12.5/\lambda_i} \tag{16}$$

$$P_w = 0.5\rho\pi R^2 (\frac{R}{\lambda})^3 C_p \omega_r^3 \tag{17}$$

$$T_m = P_w / \omega_r \tag{18}$$

$$P_G = V_{in} I_{dc} \tag{19}$$

$$T_e = P_G / \omega_r \tag{20}$$

$$J\frac{d\omega_r}{dt} = T_m - T_e \tag{21}$$

$$e_s = n_p \omega_r \psi_f \tag{22}$$

$$V_{in} = \frac{6\sqrt{3}}{\pi} e_s - \frac{6 n_p \omega_r L_s}{\pi} I_{dc} \tag{23}$$

where v is the wind velocity, R is the radius of the rotor, λ is the tip speed ratio, λ_i is an intermediate variable, β is the pitch angle, C_p is the power coefficient, P_w is the output power of the wind turbine, ρ is the air density, T_m is the mechanical torque, T_e is the electromagnetic torque, J is the moment of inertia.

References

[1] H. Y. Mahmoud, H. M. Hasanien, A. H. Besheer and A. Y. Abdelaziz, "Hybrid cuckoo search algorithm and grey wolf optimizer-based optimal control strategy for performance enhancement of HVDC-based offshore wind farms," *IET Gener. Transm. Distrib*., vol. 14, no. 10, pp. 1902-1911.

[2] X. Zeng, T. Liu, S. Wang, Y. Dong, B. Li and Z. Chen, "Coordinated control of MMC-HVDC system with offshore wind farm for providing emulated inertia support," *IET Renew. Power Gener*., vol. 14, no. 5, pp. 673-683.

[3] P. Hu, R. Teodorescu, S. Wang, S. Li and J. M. Guerrero, "A Currentless Sorting and Selection-Based Capacitor-Voltage-Balancing Method for Modular Multilevel Converters," *IEEE Trans. Power Electron.*, vol. 34, no. 2, pp. 1022-1025, Feb. 2019.

[4] A. Bidadfar, O. Saborío-Romano, J. N. Sakamuri, N. A. Cutululis, V. Akhmatov and P. E. Sørensen, "On Feasibility of Autonomous Frequency-Support Provision From Offshore HVDC Grids," *IEEE Trans. Power Del*., vol. 35, no. 6, pp. 2711-2721, Dec. 2020.

[5] N. Nityanand and A. K. Pandey, "HVDC-Based Multilevel Modular Power Converter for Offshore Wind Farms," *2018 International Conference on Power Energy, Environment and Intelligent Control (PEEIC)*, Greater Noida, India, 2018, pp. 540-544.

[6] P. Hu, R. Teodorescu and J. M. Guerrero, "Negative-Sequence Second-Order Circulating Current Injection for Hybrid MMC Under Over-Modulation Conditions," *IEEE J. Emerg. Sel. Topics Power Electron*., vol. 8, no. 3, pp. 2508-2519, Sept. 2020.

[7] A. Parastar and J. Seok, "High-Gain Resonant Switched-Capacitor Cell-Based DC/DC Converter for Offshore Wind Energy Systems," *IEEE Trans. Power Electron.*, vol. 30, no. 2, pp. 644-656, Feb. 2015.

[8] E. Apostolaki-Iosifidou, R. Mccormack, W. Kempton, P. Mccoy and D. Ozkan, "Transmission Design and Analysis for Large-Scale Offshore Wind Energy Development," *IEEE Power and Energy Technology Systems Journal.*, vol. 6, no. 1, pp. 22-31, March 2019.

[9] C. Meyer, M. Hoing, A. Peterson and R. W. De Doncker, "Control and Design of DC Grids for Offshore Wind Farms," *IEEE Trans. Ind. Appl.*, vol. 43, no. 6, pp. 1475-1482, Nov.-dec. 2007.

[10] J. Pan, S. Bala, M. Callavik and P. Sandeberg, "Platformless DC Collection and Transmission for Offshore Wind," *11th IET International Conference on AC and DC Power Transmission*., Birmingham, 2015, pp. 1-6.

[11] L. Shu *et al*., "A Resonant ZVZCS DC–DC Converter With Two Uneven Transformers for an MVDC Collection System of Offshore Wind Farms," *IEEE Trans. Ind. Electron.*, vol. 64, no. 10, pp. 7886-7895, Oct. 2017.

[12] M. Pape and M. Kazerani, “An Offshore Wind Farm with DC Collection System Featuring Differential Power Processing,” *IEEE Trans. Energy Convers.*, vol. 35, no. 1, pp. 222-236, March 2020.
[13] W. Tang, M. Shi, Z. Li and N. Yu, “Loss Comparison Study of MMC-HVDC and All-DC Offshore Wind farm,” *2019 IEEE Innovative Smart Grid Technologies - Asia (ISGT Asia)*, Chengdu, China, 2019, pp. 171-175.
[14] Max, L. and Lundberg, S., “System efficiency of a DC/DC converter-based wind farm,” *Wind Energ*., 11: 109-120., 2008.
[15] Y. Zhou, D. E. Macpherson, W. Blewitt and D. Jovcic, “Comparison of DC-DC converter topologies for offshore wind-farm application,” *6th IET International Conference on Power Electronics, Machines and Drives (PEMD 2012)*, Bristol, 2012, pp. 1-6.
[16] S. Lu, K. Sun, G. Cao, Y. Li, J. Ha and G. Min, “A High Step-Up Modular Isolated DC-DC Converter for Large Capacity Photovoltaic Generation System Integrated into MVDC Grids,” *2019 10th International Conference on Power Electronics and ECCE Asia (ICPE 2019 - ECCE Asia)*, Busan, Korea (South), 2019, pp. 1915-1920.
[17] G. Cao, Z. Guo, Y. Wang, K. Sun and H. Kim, “A DC-DC conversion system for high power HVDC-connected photovoltaic power system,” *2017 20th International Conference on Electrical Machines and Systems (ICEMS)*, Sydney, NSW, 2017, pp. 1-6, doi: 10.1109/ICEMS.2017.8056021.
[18] J. A. Ferreira, “The Multilevel Modular DC Converter,” *IEEE Trans. Power Electron.*, vol. 28, no. 10, pp. 4460-4465, Oct. 2013.
[19] S. P. Engel, M. Stieneker, N. Soltau, S. Rabiee, H. Stagge and R. W. De Doncker, “Comparison of the Modular Multilevel DC Converter and the Dual-Active Bridge Converter for Power Conversion in HVDC and MVDC Grids,” *IEEE Trans. Power Electron.*, vol. 30, no. 1, pp. 124-137, Jan. 2015.
[20] N. Denniston, A. M. Massoud, S. Ahmed and P. N. Enjeti, “Multiple-Module High-Gain High-Voltage DC–DC Transformers for Offshore Wind Energy Systems,” *IEEE Trans. Ind. Electron.*, vol. 58, no. 5, pp. 1877-1886, May 2011.
[21] K. Sano and M. Takasaki, “A boost conversion system consisting of multiple DC-DC converter modules for interfacing wind farms and HVDC transmission,” *2013 IEEE Energy Conversion Congress and Exposition*, Denver, CO, 2013, pp. 2613-2618.
[22] A. J. B. Bottion and I. Barbi, “Input-Series and Output-Series Connected Modular Output Capacitor Full-Bridge PWM DC–DC Converter,” *IEEE Trans. Ind. Electron.*, vol. 62, no. 10, pp. 6213-6221, Oct. 2015.
[23] X. Fang, H. Hu, J. Shen and I. Batarseh, “An optimal design of the LLC resonant converter based on peak gain estimation,” *2012 Twenty-Seventh Annual IEEE Applied Power Electronics Conference and Exposition (APEC)*, Orlando, FL, 2012, pp. 1286-1291.
[24] A. K. S. Bhat, “Analysis and design of a modified series resonant converter,” *IEEE Trans. Power Electron.*, vol. 8, no. 4, pp. 423-430, Oct. 1993.
[25] G. S. N. Raju and S. Doradla, “An LCL resonant converter with PWM control-analysis, simulation, and implementation,” *IEEE Trans. Power Electron.*, vol. 10, no. 2, pp. 164-174, March 1995.
[26] S. Kato, Y. Inui, M. Michihira, A. Tsuyoshi, "A Low-Cost Wind Generator System with a Permanent Magnet Synchronous Generator and Diode Rectifiers". *International Conference on Renewable Energies and Power Quality (ICREPQ'07)*, 2007, pp. 38-44.
[27] L. Max, “Energy Evaluation for DC/DC Converters in DC-Based Wind Farms.” Thesis for the degree of licentiate of engineering. PhD thesis, Department of Energy and Environment Chalmers university of technology, 2007.
[28] Half-Bridge, L. L. C. “Resonant Converter Design Using FSFR-series Fairchild Power Switch (FPS™),” Application Note AN-4151. Fairchild Semiconductor Corporation (2007).
[29] W. Li, C. Abbey and G. Joós, “Control and performance of wind turbine generators based on permanent magnet synchronous machines feeding a diode rectifier,” *2006 37th IEEE Power Electronics Specialists Conference*, Jeju, 2006, pp. 1-6.
[30] W. Chen, X. Ruan, H. Yan and C. K. Tse, “DC/DC Conversion Systems Consisting of Multiple Converter Modules: Stability, Control, and Experimental Verifications,” *IEEE Trans. Power Electron.*, vol. 24, no. 6, pp. 1463-1474, June 2009.